3A.1 A NUMERICAL MODELING STUDY OF THE NOCTURNAL BOUNDARY LAYER INSIDE ARIZONA'S METEOR CRATER

MICHAEL T. KIEFER* AND SHIYUAN ZHONG
Michigan State University, East Lansing, Michigan

1. INTRODUCTION

The development and evolution of nocturnal boundary layers within mountain basins is a subject of great interest to researchers studying, for example, air pollution in basins (Reddy et al., 1995) and aviation impacts from reduced visibility (Smith et al., 1997). A common feature of nocturnal boundary layers in basins are cold-air pools, defined as topographically confined, stagnant layers of air that are colder than the overlying air (Whiteman et al., 2001). In extreme cases, the air temperature near the surface in valleys or basins may be on the order of 10 K colder than external near-surface air (Whiteman et al., 2001).

An improved understanding of the physical processes governing the evolution of cold-air pools was a primary motivation for the METCRAX experiment conducted during October 2006 within Arizona's Meteor Crater near Winslow, Arizona (Whiteman et al., 2008). While other field studies have contributed to our understanding of stable boundary layer structure and evolution in valleys and basins (e.g., Whiteman et al., 1999; Clements et al., 2003; Steinacker et al., 2007), the METCRAX experiment was unique in terms of the idealized nature of the study area. Meteor Crater, being symmetrical in shape and exhibiting uniform slope and sidewall heights without gaps, made it an ideal site for examining boundary layer growth and evolution. The crater, formed approximately 50,000 years ago by a meteorite impact, is approximately 165 m deep and 1200 m in diameter at rim level. The rim of the crater rises approximately 50 m above the surrounding plain of the Colorado Plateau and is unbroken by large saddles or passes.

Analysis of the METCRAX data as reported in previous studies (Whiteman et al., 2008; Yao and Zhong, 2009) has revealed several aspects of the crater atmosphere for which the physical mechanisms are not well understood. First, a quasi-steady three-layer thermal structure was observed within the crater during quiescent nights (including the night of 22-23 October 2006), consisting of a strong surface inversion, an overlying nearly isothermal layer, and a secondary inversion near the top of the crater (Fig. 1). Such a structure had not been observed in prior studies of nocturnal boundary layer structures in closed basins (e.g., Clements et al., 2003). Second, a horizontally homogeneous state was observed away from the crater floor and the sidewalls, as evidenced by the nearly identical profiles measured at the three sites spanning the crater (Fig. 1). Other aspects of the crater have also been identified, including asymmetry in the inflow on the western and eastern sidewalls of the crater (Kossmann et al., 2009), and a tendency for air flowing toward the crater to pass over rather than descend into the basin (Whiteman et al., 2008; Kossmann et al., 2009). The goal of this study is to use a numerical model to first replicate, and then examine the dynamics of those observed phenomena.

2. METHOD

The numerical model utilized for this study is the Advanced Regional Prediction System (ARPS) Version 5.2.7 (Xue et al., 2000, 2003). ARPS is a three-dimensional, compressible, nonhydrostatic atmospheric modeling system with a terrain-following coordinate system. A 1.5-order subgrid-scale turbulence closure scheme with a prognostic equation for the turbulent kinetic energy is utilized, as well as a land surface and vegetation model based on Noilhan and Planton (1989) and Pleim and Xiu (1995) and radiation physics following Chou (1990, 1992) and Chou and Suarez (1994). Effects of topographic shading on radiative fluxes are accounted for as in Colette et al. (2003). Fourth-order accurate finite differencing of the advection terms is used in both the vertical and horizontal directions, while the upper boundary condition for all simulations is a sponge layer from z = 10 km to the model top at z = 12 km.

To accurately represent regional and local forcing within the region of the crater, a series of one-way nested simulations are executed, spanning from 9-km to 50-m horizontal grid spacing with an approximately 1:3 nesting ratio with each simulation initialized at 0500 MST 22 October 2006. North American Regional Reanalysis

*Corresponding author address: Michael Kiefer, Department of Geography, Michigan State University, 116 Geography Building, East Lansing, MI 48823.
E-mail: mtkiefer@msu.edu

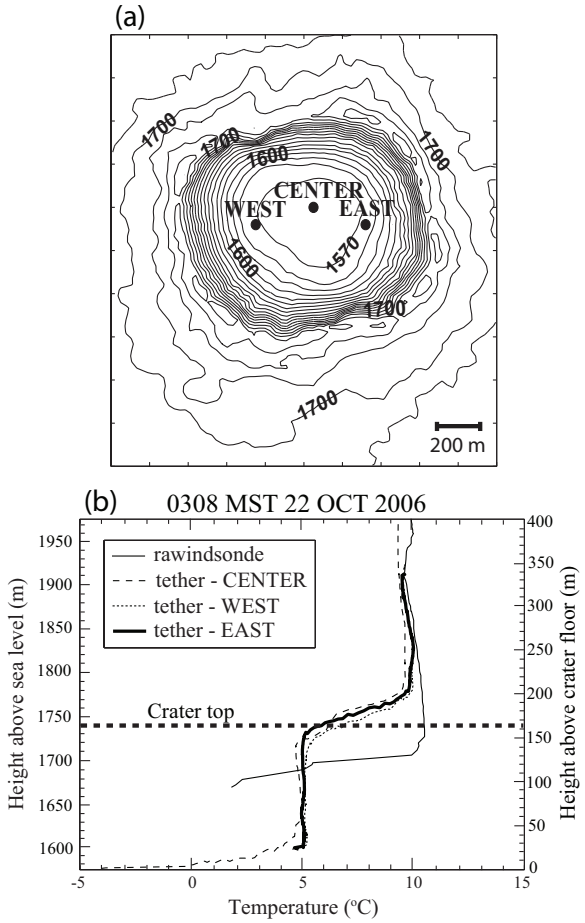

Figure 1: (a) Topographic map of Arizona's Meteor Crater with locations of tethersonde sites overlaid. (b) Coincident temperature soundings made from the west, center, and east tethersondes inside the crater and the rawindsonde outside the crater at 0308 MST 23 Oct 2006. For reference, the rawinsonde site is located approximately 5 km north-northwest of the crater. Elevation of crater rim is indicated by horizontal dashed line.

data (NARR) (Mesinger et al., 2006) is used to specify both initial and boundary conditions for the outermost grid. Land use and terrain data are input from the U.S. Geological Survey (USGS) 1-km and 100-m datasets, respectively. The outermost grid contains most of Arizona, as well as portions of New Mexico, Colorado, Utah, and Nevada, with the innermost grid consisting of a 25-km^2 area centered on the crater (Fig. 2). The model terrain does not feature a rim (see Fig. 2c) due to the relatively coarse topographic dataset used for this study. Stretching is applied along the vertical axis with a minimum vertical grid spacing of 2.5 m near the surface in the 50-m grid spacing innermost grid. The grid is gradually stretched to 300 m at the model top near 12 km above mean sea level (MSL).

3. RESULTS

a. Crater Atmosphere Characteristics

Before proceeding to examine the dynamics of the model crater atmosphere, it is important to assess the ability of the model to reproduce the observed crater characteristics described earlier: a three-layer thermal structure, approximate horizontal homogeneity, asymmetry between upslope and downslope flows, and a tendency for katabatic flow to spill over the crater rather than descend into it. Regarding the three-layer thermal structure, it is apparent from Fig. 3 that the model is able to reproduce the phenomenon. One can see that two inversions are present in the temperature profile at 2000 MST 22 October (hereafter, 2000 MST), one spanning the lowest 10-15 m of the crater, and the second beginning near the height of the model crater top and extending approximately 50 m upward. The layer between the two inversions exhibits much weaker potential temperature lapse rates and is, in fact, near isothermal. Accounting for the cold bias in the initial condition and the shallow crater depth, the model does reasonably capture the three-layer structure. Note that although the three-layer structure is also present later at 2300 and 0200 MST (not shown), periods of time do exist during the night when the isothermal layer is replaced with a somewhat more stable layer.

In order to better examine the structure of the model crater atmosphere, vertical cross sections of potential temperature are presented in Fig. 4. During the first 1-2 hours following astronomical sunset, the potential temperature of the drainage flow approaching the crater is colder than the potential temperature at the same elevation inside the crater (Fig. 4a). Thus, negatively buoyant air pours into the crater, contributing to the cold pool at the basin floor, while compensating vertical advection cools the crater atmosphere away from the floor and sidewalls. It is worth noting that during the period 1700-1900 MST, when intrusion of air into the crater is most

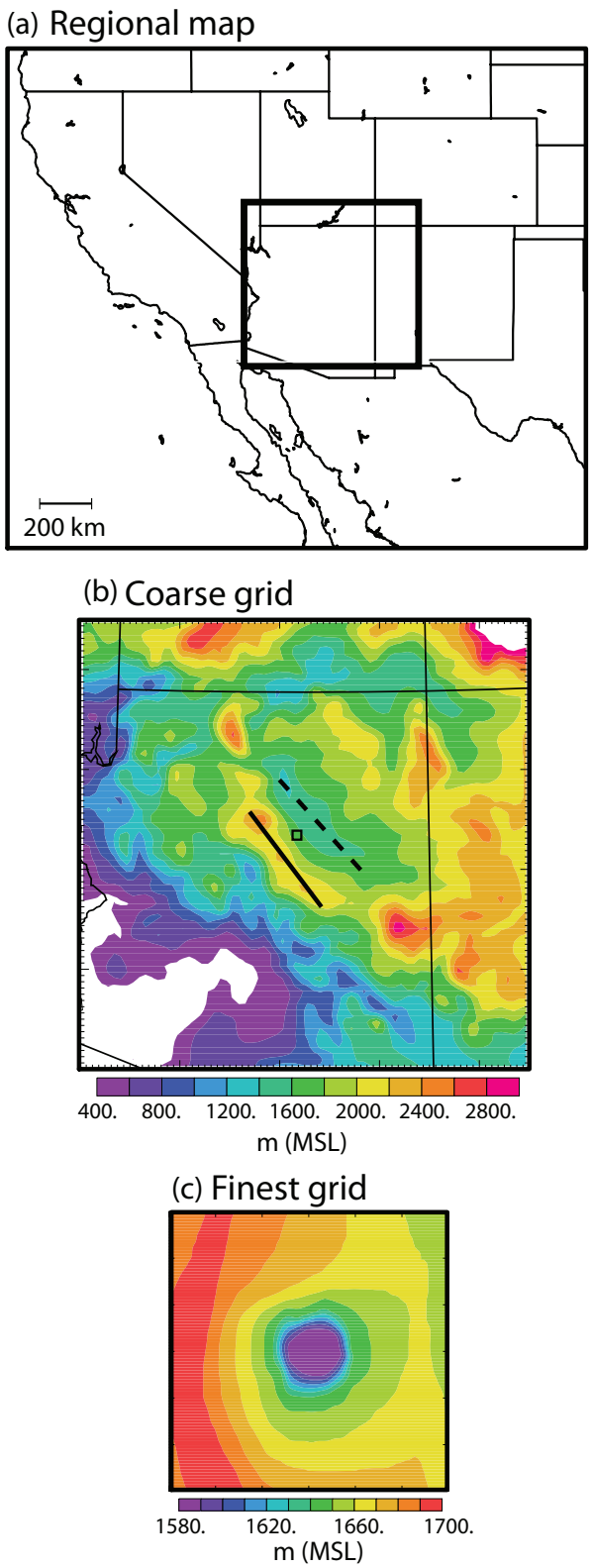

Figure 2: Summary of grid nesting strategy: (a) political map of the southwestern U.S. with outermost grid domain outlined, and surface elevation maps of the (b) outermost and (c) innermost grid domains. Axes of principal topographic features in the vicinity of the crater are marked in panel (b): Mogollon Rim - solid line; Little Colorado River Valley - dashed line.

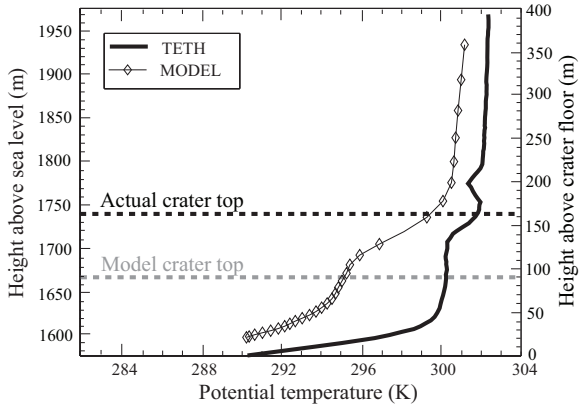

Figure 3: Vertical profiles of potential temperature (K) at 2000 MST 22 Oct 2006 (0300 UTC 23 Oct 2006), valid in crater center. TETH profiles corresponds to tethersonde observations from the METCRAX experiment and MODEL refers to the ARPS simulation. Elevation of actual and model crater top indicated by horizontal black and gray dashed lines, respectively; differences in crater top elevation result from the relatively coarse (100 m) resolution of the terrain dataset.

robust, inflow occurs predominately along the western sidewall (i.e., the inflow is asymmetric).

By 2000 MST, the crater atmosphere has cooled to the point where approaching air is neutrally buoyant with respect to the air at the same elevation inside the crater, and the incoming air sweeps across the top of the basin (Fig. 4b). Although differences between the atmosphere inside the crater and over the surrounding plain are initially small (Fig. 4a), the crater atmosphere evolves into a three-layer structure by 2000 MST (Fig. 4b). It is also important to note the horizontally homogeneous nature of the crater atmosphere at 2000 MST (Fig. 4b) and especially at 2200 MST (Fig. 4c). Apart from the area immediately adjacent to the sidewalls, the vertical thermal structure within the crater is largely independent of location.

b. Thermodynamic Budget

With satisfactory reproduction of the salient features of the crater atmosphere during IOP5, discussion now proceeds to examination of the budgets of the thermodynamic equation. Such work allows one to better understand the atmospheric processes that yield notable characteristics of the crater atmosphere (e.g., the three layer thermal structure). First, we consider the ARPS thermodynamic equation in the absence of precipitation processes, written as

$$\frac{\partial \theta'}{\partial t} = -\mathbf{u} \bullet \nabla\theta + \nabla \bullet \mathbf{H} + R \qquad (1)$$

where we have neglected in Eq. (1) coordinate transformation factors in the ARPS prognostic equations (how-

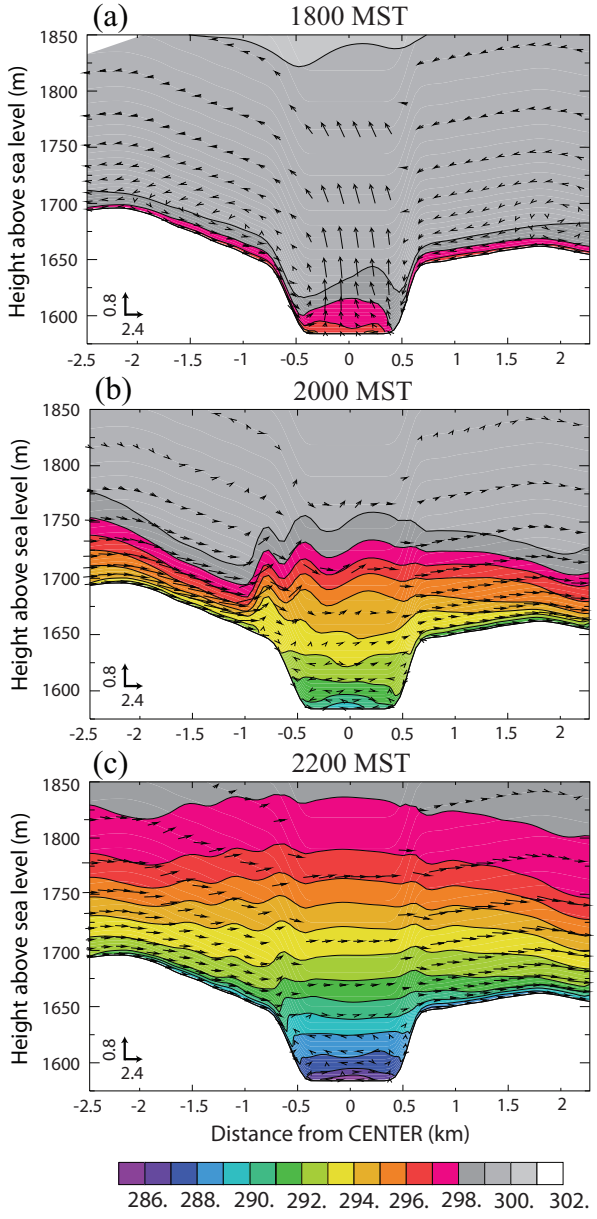

Figure 4: Vertical cross sections of potential temperature (shaded and contoured; K) and 3D wind vectors projected onto the x-z plane (m s^{-1}) for (a) 1800 MST, (b) 2000 MST, and (c) 2200 MST 22 Oct 2006. Cross section is oriented west-east through the center of crater at point CENTER. The crater extends 0.6 km to the west and east of the position marked 0 on the x-axis; note that the surrounding plains exhibit much more gently sloping terrain (∼3% slope). The vector key is provided in the lower-left corner of each panel.

ever, they are included in calculated budget terms). In Eq. (1), θ refers to potential temperature, $\bar{()}$ and $()'$ refer to base state (function of height only) and perturbation variables, $\mathbf{u}$ is the total wind vector, and $\mathbf{H}$ is the three-dimensional turbulent heat flux. Heat flux is computed in ARPS as $\mathbf{H} = \bar{\rho} K_H (\boldsymbol{\nabla} \theta)$, where $\bar{\rho}$ is base state density and K_H is the thermal turbulent diffusivity. From left to right in Eq. (1), the terms are time rate of change, or tendency, of perturbation potential temperature (TEND), advection (ADV), turbulent mixing (MIX) and radiative forcing (RAD).

During the overnight hours of 22-23 October, potential temperature profiles at CENTER frequently exhibit the three layer structure, although periods of time exist in which the isothermal layer is very shallow or lacking altogether (Fig. 5). Similar temporal variability in the thermal structure is present in the observed tethersonde profiles [See Fig. 10 in Whiteman et al. (2008)]. Comparison of the forcing terms in the thermodynamic equation between a time period when a well-developed three layer structure is present (e.g., 2000 MST) and a time period when such a structure is lacking (e.g., 2200 MST) can help shed light on how the three layer structure develops. Thus, Fig. 6 presents profiles of the thermodynamic equation forcing terms at CENTER, averaged over two one-hour periods: 1930-2030 MST (Fig. 6a,c,e) and 2130-2230 MST (Fig. 6b,d,f).

Overall, differences in forcing between the two time periods are limited to the upper part of the crater crater atmosphere and adjacent free atmosphere (roughly above 1670 m MSL). At the surface, steady cooling of near surface air during both time periods occurs due to MIX, dominated by the vertical component (MIX_V; not shown). Such notable flux divergence results from very weak turbulent flux in the crater and substantial sensible heat flux at the surface (not shown), consistent with a number of previous studies of cold-air pool development in sheltered valleys and basins (e.g., Vosper and Brown, 2008; Gustavsson et al., 1998). Away from the immediate surface, significant changes in the vertical structure of the forcing terms occur between 1930-2030 MST and 2130-2230 MST (cf. Figs. 6a and 6b). During the 1930-2030 MST time period, strong cooling centered in the 1650-1700 m MSL layer occurs via advective forcing, with weaker cooling below. Thus, during this stage, air cools disproportionately more near 1685 m MSL than it does near 1620 m MSL, consistent with the relatively weak stability in the upper half of the crater (i.e., the isothermal layer). Examination of the components of ADV reveals that large magnitudes of ADV_H and ADV_V are present during 1930-2030 MST in the layer between 1650 and 1800 m MSL (Fig. 7). The locally strong cooling noted in Fig. 6a near the top of the isothermal layer is the result of a slight imbalance be-

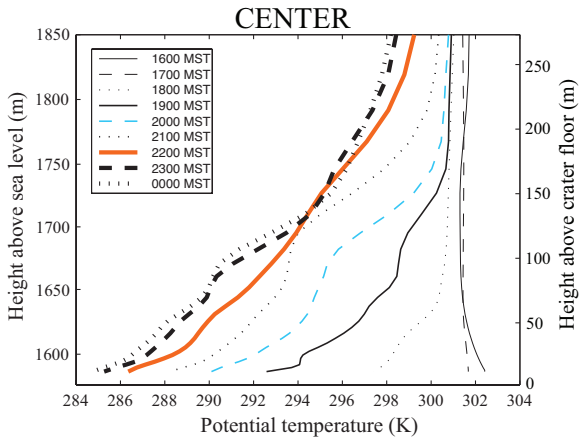

Figure 5: Vertical profiles of potential temperature for period 1600 MST 22 October - 0000 MST 23 October, at point CENTER. Line thickness varies between profiles; Light: 1600-1800 MST; Medium: 1900-2100 MST; Heavy: 2200-0000 MST. Times corresponding to averaged periods examined in Fig. 6 indicated by colored lines: turquoise (1930-2030 MST); orange (2130-2230 MST). See legend for details.

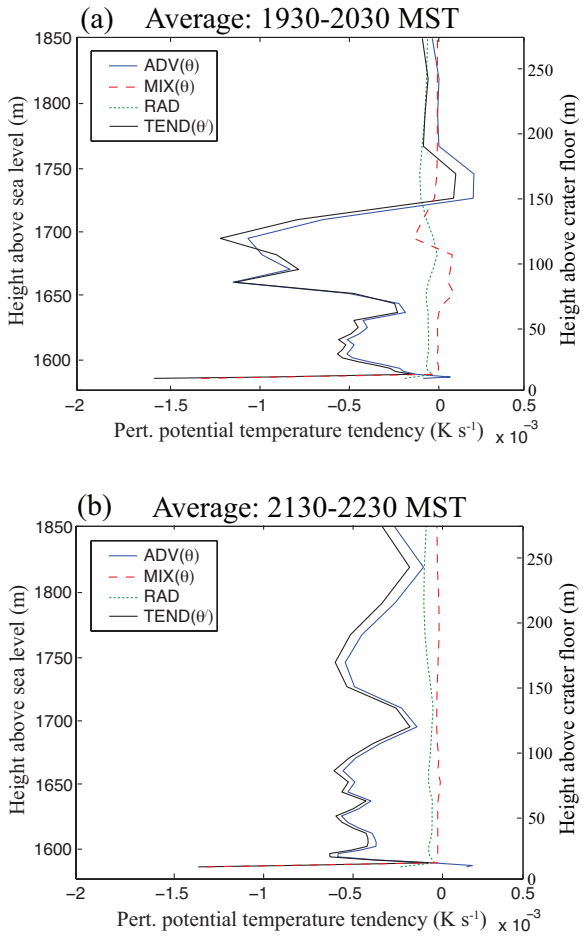

Figure 6: Vertical profiles of total forcing terms in thermodynamic equation at point CENTER. Profiles are temporally averaged: (a) 1930-2030 MST and (b) 2130-2230 MST 22 October 2006. Perturbation potential temperature tendency term (TEND) is calculated as the sum of the forcing terms; See text and Eq. (1) for description.

tween ADV_H and ADV_V.

Further examination reveals that the layer of strong cooling near 1685 m MSL corresponds to a layer of westerly flow with embedded gravity waves (cf. Fig 4b and Fig. 6a). In this layer, cold air from the lower atmosphere upstream of the crater is advected across the top of the basin. By the 2130-2230 MST period, however, strong advective cooling in the layer above the crater is absent. Note that the role of advection in destabilizing nocturnal boundary layers in basins has been documented before, for example, in Whiteman et al. (2001) in the Columbia River basin of eastern Washington. However, turbulent mixing, either associated with vertical wind shear near the crater top, as proposed by Kossmann et al. (2009), or adjacent to the sidewalls where cold air entrainment occurs (Whiteman et al., 2009, 2010), does not appear to play a significant role in destabilizing the crater atmosphere in these simulations.

4. DISCUSSION

The prevalence of regional-scale cold-air flows at night in the vicinity of Meteor Crater (Savage et al., 2008) and the geometry of the crater suggests that the three-layer structure described in this paper is not an isolated occurrence (Whiteman et al., 2010). In fact, Savage et al. (2008) found that southwesterly downslope flow was present at night over the plains surrounding Meteor Crater more than 50% of the time during October 2006, most commonly under quiescent synoptic conditions. Climatic studies have shown that ridges of high pressure are present in the southwestern United States

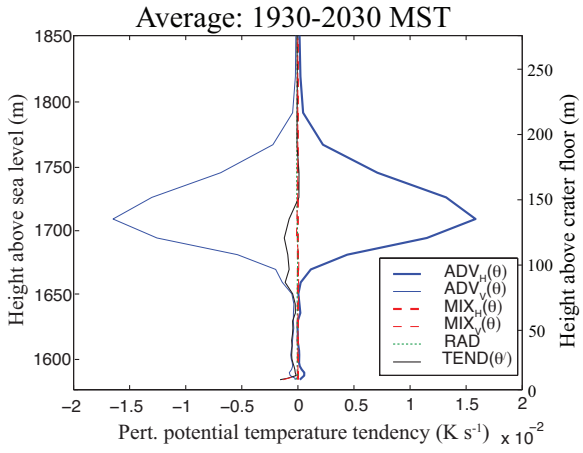

Figure 7: As in Fig. 6a, but with horizontal and vertical components of terms in thermodynamic equation.

on more than 70% of the days during the summer and early autumn (Wang and Angell, 1999); stable, calm conditions have been shown to be highly favorable for development of regional-scale terrain-induced circulations. The IOP5 (22-23 Oct) case was chosen for this study because it is the best example of a quiescent night with the three-layer thermal structure observed during METCRAX. However, the phenomenon was also observed on several other nights during the field campaign (not shown). The advection mechanism that our study proposes for the cause of the isothermal layer (i.e., the middle part of the three-layer structure) is dependent on the presence of the regional-scale drainage flow. Thus, we expect that the mechanism is probably active on most nights with quiescent conditions, that is, without the influence of broader-scale phenomena such as upper-level troughs or cold fronts. Further, even on nights where large-scale phenomena does disrupt the regional-scale drainage flow, such as during IOP 4, the three-layer structure may be present during at least part of the overnight when regional-scale flow is able to develop (Whiteman et al., 2010). Lastly, similar boundary layer structure is expected to occur in other basins in the western U.S. and other mountainous regions of the world.

5. CONCLUSIONS

This numerical modeling study has examined the evolution of the nocturnal boundary layer observed within Arizona's Meteor Crater during the METCRAX field campaign IOP 5 (22-23 October 2006). Four aspects of the observed crater atmosphere were investigated: a quasi-steady state three-layer temperature structure, horizontal homogeneity of the crater atmosphere, asymmetric inflow, and the tendency for katabatic flow to spill over rather than descend into the crater. Despite limitations of the modeling strategy, including the relatively coarse terrain dataset ($\Delta x \sim 100$ m) and incomplete model radiation physics, the numerical simulations were able to reproduce the salient features of the nocturnal boundary layer. Subsequent analysis of the model thermodynamic forcing terms provided valuable clues as to the source of the observed aspects of the crater atmosphere (e.g., the three-layer structure).

Figure 8 presents a conceptual model of the isothermal process investigated in this study. At the onset of the isothermal stage, cold-air pool development has evolved to the point where the incoming drainage flow is no longer colder than the air at the same elevation within the crater. Thus, the cold-air flow is redirected laterally across the top of the basin cold-air pool, triggering the development of gravity waves immediately above the cold-air pool. The gravity wave activity is embedded within a layer of westerly flow in which cold air from

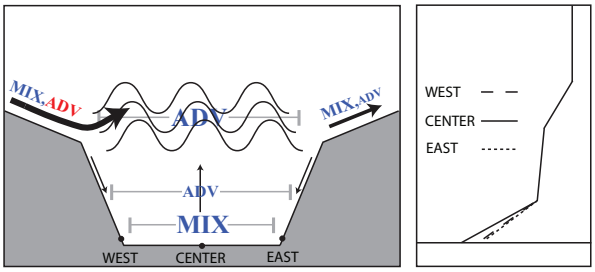

Figure 8: Schematic depiction of dominant thermodynamic forcing during development of isothermal layer. Left panel depicts west-east cross-section of crater with dominant thermodynamic forcing (see Eq. (1) for definition of terms) and typical air flow into and out of the crater indicated, and right panel depicts potential temperature profiles at several points in crater (points correspond approximately to locations in Fig. 1). Red (blue) font used to indicate forcing of positive (negative) sign. Relative magnitude of forcing indicated by size of text, and relative strength of wind indicated by thickness of arrows. Location of gravity waves indicated. See text for full description of schematic.

the lower atmosphere upstream of the crater is advected above the top of the basin. Cooling associated with cold air advection at the top of the crater is stronger than the cooling taking place within the basin interior; differential cooling of the crater atmosphere thus destabilizes the boundary layer, yielding an isothermal layer. Cooling due to turbulent flux divergence is mainly limited to near the crater floor.

In spite of the stated limitations of this study, results presented in this paper represent an important step in improving our understanding of nocturnal boundary layer evolution in closed basins. The main contribution to the knowledge base from this study is the new mechanism for generating an isothermal layer inside small closed basins. More generally though, our study provides additional insight into how airflow outside of a closed basin can impact the boundary layer structure inside. Ongoing work involves performing idealized simulations of the atmosphere in Meteor Crater in order to examine the impact of the crater rim on the nocturnal boundary layer structure. More generally, further analysis of field observations and model results are expected to yield large advances in our knowledge of the boundary layer in complex terrain.

ACKNOWLEDGMENTS

We wish to thank the National Center for Atmospheric Research (NCAR) staff for providing equipment, field support and data processing, and the Barringer Crater Corporation and Meteor Crater Enterprises, Inc. for providing crater access, during the METCRAX experiment. This research was supported by the U.S. National Science Foundation Physical and Dynamic Meteorology Division (A. Detwiler, Program Manager) through Grant 0837860. Any opinions, findings, and conclusions or recommendations expressed are those of the authors and do not necessarily reflect the views of the National Science Foundation. All simulations were performed on the NCAR supercomputer

Bluefire, managed and operated by the Computational and Information Systems Laboratory (CISL)

REFERENCES

Chou, M.-D., 1990: Parameterization for the absorption of solar radiation by O_2 and CO_2 with application to climate studies. *J. Climate*, **3**, 209–217.

Chou, M.-D., 1992: A solar radiation model for climate studies. *J. Atmos. Sci.*, **49**, 762–772.

Chou, M.-D., and M. J. Suarez, 1994: An efficient thermal infrared radiation parameterization for use in general circulation models. NASA Tech. Memo 104606, 85 pp. [Available from NASA Center for Aerospace Information, 800 Elkridge Landing Road, Linthicum Heights, MD 21090-2934]

Clements, C. B., C. D. Whiteman, and J. D. Horel, 2003: Cold-air-pool structure and evolution in a mountain basin: Peter Sinks, Utah. *J. Appl. Meteor.*, **42**, 752–768.

Colette, A. G., F. Katopodes Chow, and R. L. Street, 2003: A numerical study of inversion-layer breakup and the effects of topographic shading in idealized valleys. *J. Appl. Meteor.*, **42**, 1255–1272.

Gustavsson, T., M. Karlsson, J. Bogren, and S. Lindqvist, 1998: Development of temperature patterns during clear nights. *J. Appl. Meteor.*, **37**, 559–571.

Kossmann, M., S. W. Hoch, C. D. Whiteman, and U. Sievers, 2009: Modeling of nocturnal drainage winds at meteor crater, arizona using KLAM_21. Preprints, *30th International Conference on Alpine Meteorology*, Rastatt, Germany, 182–183.

Mesinger, F., G. DiMego, E. Kalnay, K. Mitchell, P. C. Shafran, W. Ebisuzaki, D. Jovic, J. Woollen, E. Rogers, E. H. Berbery, M. B. Ek, Y. Fan, R. Grumbine, W. Higgins, H. Li, Y. Lin, G. Manikin, D. Parrish, and W. Shi, 2006: North American Regional Reanalysis. *Bull. Amer. Meteor. Soc.*, **87**, 343–360.

Noilhan, J., and S. Planton, 1989: A simple parameterization of land surface processes for meteorological models. *Mon. Wea. Rev.*, **117**, 536–549.

Pleim, J. E., and A. Xiu, 1995: Development and testing of a surface flux and planetary boundary layer model for application in mesoscale models. *J. Appl. Meteor.*, **34**, 16–32.

Reddy, P. J., D. E. Barbarick, and R. D. Osterburg, 1995: Development of a statistical model for forecasting episodes of visibility degradation in the Denver metropolitan area. *J. Appl. Meteor.*, **34**, 616–625.

Savage, L. C., S. Zhong, W. Yao, W. J. O. Brown, T. W. Horst, and C. D. Whiteman, 2008: An observational and numerical study of a regional-scale downslope flow in northern Arizona. *J. Geophys. Res.*, **113**, D14114.

Smith, R. B., J. Paegle, T. Clark, W. Cotton, D. Durran, G. Forbes, J. Marwitz, C. Mass, J. McGinley, H. L. Pan, and M. Ralph, 1997: Local and remote effects of mountains on weather: Research needs and opportunities. *Bull. Amer. Meteor. Soc.*, **78**, 877–892.

Steinacker, R., C. D. Whiteman, M. Dorninger, E. Mursch-Radlgruber, K. Baumann, S. Eisenbach, A. M. Holzer, and B. Pospichal, 2007: A sinkhole field experiment in the Eastern Alps. *Bull. Amer. Meteor. Soc.*, **88**, 701–716.

Vosper, S. B., and A. R. Brown, 2008: Numerical simulations of sheltering in valleys: The formation of nighttime cold-air pools. *Bound.-Layer Meteor.*, **127**, 429–448.

Wang, J. X. L., and J. K. Angell, 1999: Air stagnation climatology for the United States (1948-1998). NOAA/Air Resources Laboratory ATLAS No. 1, 73 pp.

Whiteman, C. D., S. W. Hoch, and M. Lehner, 2009: Nocturnal cold air intrusions at Arizona's Meteor Crater. Preprints, *30th International Conference on Alpine Meteorology*, Rastatt, Germany, 96–97.

Whiteman, C. D., S. W. Hoch, M. Lehner, and T. Haiden, 2010: Nocturnal cold air intrusions into a closed basin: Observational evidence and conceptual model. *J. Appl. Meteor. Climatol.*, **999**, In Press.

Whiteman, C. D., A. Muschinski, S. Zhong, D. Fritts, S. W. Hoch, M. Hahnenberger, W. Yao, V. Hohreiter, M. Behn, Y. Cheon, C. B. Clements, T. W. Horst, W. O. J. Brown, and S. P. Oncley, 2008: Metcrax 2006 - Meteorological experiments in Arizona's Meteor Crater. *Bull. Amer. Meteor. Soc.*, **89**, 1665–1680.

Whiteman, C. D., S. Zhong, and X. Bian, 1999: Wintertime boundary layer structure in the Grand Canyon. *J. Appl. Meteor.*, **38**, 1084–1102.

Whiteman, C. D., S. Zhong, W. J. Shaw, J. M. Hubbe, X. Bian, and J. Mittelstadt, 2001: Cold pools in the columbia basin. *Wea. Forecasting*, **16**, 432–447.

Xue, M., K. K. Droegemeier, and V. Wong, 2000: The Advanced Regional Prediction System (ARPS) – A multi-scale nonhydrostatic atmosphere simulation and prediction model. Part I: Model dynamics and verification. *Meteor. Atmos. Phys.*, **75**, 463–485.

Xue, M., D. Wang, J. Gao, K. Brewster, and K. K. Droegemeier, 2003: The Advanced Regional Prediction System (ARPS), storm-scale numerical weather prediction and data assimilation. *Meteor. Atmos. Phys.*, **82**, 139–170.

Yao, W., and S. Zhong, 2009: Nocturnal temperature inversions in a small, enclosed basin and their relationship to ambient atmospheric conditions. *Meteor. Atmos. Phys.*, **103**, 195–210.